DTIC FILE COPY

Naval Research Laboratory

Washington, DC 20375-5000

AD-A200 189

Aneurisms in Laser-Driven Blast Waves

J. A. STAMPER AND B. H. RIPIN

Laser Plasma Branch
Plasma Physics Division

R. E. PETERKIN, JR. AND R. F. STELLINGWERF

Mission Research Corporation
Albuquerque, NM 87106

DTIC
SELECTED
OCT 0 7 1988
D

August 25, 1988

REPORT DOCUMENTATION PAGE

Form Approved
OMB No 0704-0188

1a REPORT SECURITY CLASSIFICATION UNCLASSIFIED	1b RESTRICTIVE MARKINGS

2a SECURITY CLASSIFICATION AUTHORITY	3 DISTRIBUTION/AVAILABILITY OF REPORT
2b DECLASSIFICATION/DOWNGRADING SCHEDULE	Approved for public release; distribution unlimited.

4 PERFORMING ORGANIZATION REPORT NUMBER(S) NRL Memorandum Report 6184	5 MONITORING ORGANIZATION REPORT NUMBER(S)

6a NAME OF PERFORMING ORGANIZATION Naval Research Laboratory	6b OFFICE SYMBOL (If applicable) Code 4730	7a NAME OF MONITORING ORGANIZATION

6c. ADDRESS (City, State, and ZIP Code) Washington, DC 20375-5000	7b ADDRESS (City, State, and ZIP Code)

8a. NAME OF FUNDING/SPONSORING ORGANIZATION Defense Nuclear Agency	8b OFFICE SYMBOL (If applicable)	9 PROCUREMENT INSTRUMENT IDENTIFICATION NUMBER

8c. ADDRESS (City, State, and ZIP Code) Washington, DC 20305	10 SOURCE OF FUNDING NUMBERS

PROGRAM ELEMENT NO	PROJECT NO	TASK NO	WORK UNIT ACCESSION NO

11 TITLE (Include Security Classification)

Aneurisms in Laser-Driven Blast Waves

12. PERSONAL AUTHOR(S)
Stamper, J.A., Ripin, B.H., Peterkin, R.E. Jr.,* and Stellingwerf, R.F.*

13a TYPE OF REPORT Interim	13b TIME COVERED FROM _____ TO _____	14 DATE OF REPORT (Year, Month, Day) 1988 August 25	15 PAGE COUNT 46

16 SUPPLEMENTARY NOTATION
*Mission Research Corporation, Albuquerque, NM 87106

17 COSATI CODES			18 SUBJECT TERMS (Continue on reverse if necessary and identify by block number)
FIELD	GROUP	SUB-GROUP	Laser, Plasmas,
			Aneurisms, Shadowgraphy, (j b d)
			Simulation

19 ABSTRACT (Continue on reverse if necessary and identify by block number)

When a short-pulse laser beam is focused onto a solid target in a few Torr ambient gas, the expanding target plasma couples to the resulting ambient plasma. Dark-field shadowgrams show that a thin, nearly-spherical blast front is produced. These shadowgrams also show that certain regions of the blast front (called aneurisms) may project well ahead of the neighboring, spherical part. Several mechanisms for aneurisms are discussed. One class of aneurisms is consistently produced along the laser axis when the laser energy is greater than about 10 Joules. Two-dimensional, hydrodynamic computer simulations of these on-axis aneurisms show that they can be accounted for by the laser heating of an on-axis channel.

Laser, Tour interact...

20 DISTRIBUTION AVAILABILITY OF ABSTRACT ☒ UNCLASSIFIED UNLIMITED ☐ SAME AS RPT ☐ DTIC USERS	21 ABSTRACT SECURITY CLASSIFICATION UNCLASSIFIED
22a NAME OF RESPONSIBLE INDIVIDUAL John A. Stamper	22b TELEPHONE (Include Area Code) (202) 767-2730	22c OFFICE SYMBOL Code 4730

DD Form 1473, JUN 86   Previous editions are obsolete   SECURITY CLASSIFICATION OF THIS PAGE

S/N 0102-LF-014-6603

CONTENTS

DTIC
COPY
INSPECTED
6

Accesion For

NTIS   CRA&I   ☑
DTIC   TAB   ☐
Unannounced   ☐
Justification

By
Distribution /

Availability Codes

Dist   Avail and / or
       Special

A-1

ANEURISMS IN LASER-DRIVEN BLAST WAVES

I. Introduction

When a powerful, short-pulsed laser beam is focused onto a solid target located in a low-pressure ambient gas, two interstreaming plasmas are produced. The target plasma is produced directly by the absorption of laser energy near the critical surface and streams radially away from the focal region. The ambient gas is also ionized near the target by energetic photons emitted from the target plasma. At high ambient pressures ($\gtrsim 1$ Torr), the expanding target plasma collisionally couples to the initially-stationary ambient plasma so that, for times long compared to the laser pulse width, a thin nearly-spherical blast front is produced.[1] The ambient plasma is further ionized by radiation and collisions from the blast front. Although blast fronts are normally considered to be hydrodynamically stable,[2] we have observed (in dark-field shadowgrams) regions of the blast front projecting well ahead of the neighboring, spherical part. These projections are termed "aneurisms."

Although more than one mechanism is responsible for aneurism production, one class is consistently produced along the laser axis when the laser energy and ambient pressure are sufficiently high. Two-dimensional hydrodynamic computer simulations show that these on-axis aneurisms can be accounted for by laser heating of an on-axis channel of photoionized ambient plasma. This mechanism for aneurism formation is discussed in detail

in Sections IV and V after describing a family of experiments in Section II and a general discussion of how the experimental results relate to the blast fronts and aneurisms in Section III. In Section VI, we discuss the nature of the laser-induced cylindrical shock.

II. Experimental Conditions and Diagnostics

The blast fronts are produced by focusing one of the NRL Pharos III Nd-glass laser beams (FWHM ~ 4 nsec) onto thin foil targets, initially located in a low-pressure (1-10 Torr) ambient gas. The ambient gas is usually nitrogen. The targets are typically 4 to 25 micron thick foils of aluminum or CH plastic. Laser pulses varying from a few to nearly 300 Joules are focused to a diameter in the range of one-fifth to one millimeter, producing irradiances in the range 10^{12} to 10^{14} W/cm^2. Under these conditions, the target material ablates and yields reproducible, narrow ($0.1 < \Delta V/V < 1.0$) ion velocity distributions[3] with mean velocity of a few times 10^7 cm/sec. For most of the experiments reported here $V \approx 5 \times 10^7$ cm/s with $\Delta V/V = 0.25$.

A wide variety of laser beam and target-interaction diagnostics were used, including a short-pulse probing laser beam, visible and near-UV spectroscopy, x-ray pinhole cameras and ion time-of-flight detectors. The experimental arrangement for laser probing is illustrated in Fig. 1. A short-pulse (100-300 psec), second-harmonic (5270 A) probing laser beam, time

synchronized with the main laser beam, is passed parallel to the target surface. Dark-field shadowgraphy and shearing interferometry were used to study the blast-front structure. A detailed discussion of these and other probing diagnostics is given in Ref. 4. Two lenses, separated by the sum of their focal lengths, are used in the collection optics. The target is at the front focus of the first lens and the film at the back focus of the second lens. For dark-field shadowgraphy, a razor edge is placed at the back focus of the first lens. Since most of the undeflected probe light remains collimated as it passes through the target region, it is focused onto the razor edge and blocked. This leaves a dark background, or field, on the film. However, the light that passes through steep-gradient regions, including the blast-front, is angularly scattered. This light is collimated by the first lens, misses the razor edge, and is then refocused onto the film by the second lens to produce a bright image of the steep density gradient regions on the dark background. The dark field permits multiple images to be taken on a single shot. Typically, shadowgrams are taken at two times on a given shot. For interferometry (not shown in Fig. 1), the razor edge is removed and a shearing plate is inserted at 45 degrees after the second lens. Interference between the front and rear surface reflections from the shearing plate produces an interferogram.

III. Experimental Results and Discussion of Aneurism-Producing Mechanisms

The blast-fronts and aneurisms were observed, under a wide variety of conditions, using dark-field shadowgraphy and shearing interferometry. A large, growing aneurism is seen in the dual-time, dark-field shadowgram shown in Fig. 2a. Here, a 109 Joule laser pulse was incident from the right onto a thin foil aluminum target in a 5 Torr ambient of nitrogen. The target was supported at the tip of a drawn-down glass stalk. The blast-front and a large, on-axis aneurism are seen evolving between the times (71 and 146 nsec) in the shadowgram. The blast front is slowing down as it picks up ambient mass, but the aneurism is still growing.

By observing the blast-front aneurisms in a large number of such single and dual-time, dark-field shadowgrams, we were able to see several trends. The aneurisms were generally observed at higher ambient pressures ($\gtrsim 1$ Torr), and at later times ($\gtrsim 50$ nsec). They were usually located near the laser axis but sometimes occurred well off-axis. It became clear that more than one mechanism was likely involved. Some possible mechanisms are discussed and shadowgraphy results presented to support two such mechanisms.

We have studied several target, laser, and ambient conditions which could affect aneurism production. We were particularly interested in conditions which would give a localization or

4

preferred direction for part of the blast front. The axis of the main laser beam and the target normal are two such preferred directions.

We considered hot spots in the laser beams and preferred heating along the laser axis. We found that laser beam hot spots (e.g., $\Delta I/I \sim 2$) do not play a major role in on-axis aneurism production since a variety of aneurisms were still produced when a very smooth laser beam ($\Delta I/I < 0.1$) was used. The high degree of transverse spatial smoothing of the focused beam was produced by the induced-spatial-incoherence (ISI) technique.[5] We were led to laser heating of a channel along the laser axis[6] as a dominant mechanism for the large on-axis aneurisms. To examine this mechanism it is instructive to look at times shortly after the main laser beam strikes the target. For instance, evidence of this mechanism is seen in the dark-field shadowgram taken at 16 ns, shown in Fig. 2b. For this shot, a thin-foil (8.5 micron), CH plastic target was stretched across an opening in the target holder with the target in a 5 Torr ambient of nitrogen. There was 245 Joules of ISI-smoothed laser energy incident. The time was early enough that a resolvable blast-wave had not yet developed. The ablatively-accelerated dense target plasma is seen in the gap on the left and a strong probe light scattering region is seen just right of the target. The most interesting features for understanding aneurism production are the two narrow horizontal lines, seen at the far right, on either side of the

laser axis. This is a cylindrical shock expanding about the laser beam axis, whose role in the laser-heated channel mechanism will be examined in detail in the next sections.

Further evidence for the laser-heated channel mechanism is given in the shadowgram shown in Fig. 3a. This dark-field shadowgram was taken at 59 nsec in a 5 Torr ambient of nitrogen with 95 Joules of ISI-smoothed laser energy incident. The 25-micron thick aluminum target was tilted 30 degrees from the vertical to give a clear separation between the laser axis and the target normal. Ignore the magnetic probe structure, coming in from the lower right, and the circular mask centered at the target location, used in another diagnostic. Note that there is a well-developed, on-laser-axis aneurism, expected from a laser-heated channel mechanism. The turbulent and rippled structure seen inside the blast front in these shadowgrams is not well understood at the present time.

Target size, mass, and orientation affect the direction, angular distribution and temporal history of the expanding target plasma. Thus, variations in the targets can be used to check for target-plasma contributions to aneurism mechanisms. We found that aneurisms were still produced when very thin (ablated through during the main laser probe), or limited-mass (thin disc targets of about a focal diameter) targets were used. This demonstrates that on-axis aneurism production does not necessarily depend on extraneous target mass not ablated during

6

the laser pulse. It has been suggested[7] that a localized jet of slow target material could provide a mechanism for aneurism production. As the blast front slows down, by ambient gas mass accretion, the localized jet could catch up to produce an aneurism. This mechanism may be operative for aneurisms oriented normal to the target surface. Although, as was shown in Fig. 3a, large on-axis aneurisms were consistently produced for laser energies greater than about 10 Joules, the situation is different at lower energies. The shadowgram of Fig. 3b was taken at 64 nsec in a 5 Torr ambient of nitrogen with only 3.4 Joules of ISI-smoothed laser energy on target. There is a pronounced aneurism growing along the target normal. This is what one would expect for the target jet mechanism since the target normal is the preferred direction of target plasma expansion. Evidently, the laser intensity has a lower threshold for seeding an on-axis aneurism.

Another possible aneurism mechanism is within the blast front itself. The deceleration of the blast front is high and can be several times 10^{14} cm/sec^2. Thus, hydrodynamic instability of the blast front is a consideration. Although blast waves are normally considered to be hydrodynamically stable,[2] adverse density gradients (acceleration antiparallel to the density gradient) could develop in the blast front due to local conditions in the front (e.g., conductive or radiative cooling). If the blast front were Rayleigh-Taylor unstable, the growth

7

times could be as short as ten nanoseconds.[1] Indeed, some of the blast fronts at later times and lower laser energies show a complicated break-up which may be hydrodynamic in origin. An example of such a break-up is seen in the dual-time (52, 96 nsec), dark-field shadowgram shown in Fig. 4. Here, the laser energy was 4.1 Joules and the ambient was 5 Torr of 90% N_2, 10% H_2 - with H_2 added for spectroscopic diagnostics.

Another blast-front dependent mechanism has been proposed[8] which depends on a localized thermal evaporation of the interior of the blast front and consequent preferred ablative acceleration of that region. Here, a thermal conduction front is proposed between the inner surface of the blast front and hot plasma interior. Self-generated magnetic fields,[9] which are azimuthal about a central axis and maximize off axis, provide a degree of thermal insulation on the side of the blast front but not on-axis where the fields are null. Thus, the interior of the blast front ablates more and pushes out an aneurism. We observe, in studies without ISI, large aneurisms which grow in a direction different from both the laser axis and target axis. The thermal evaporation model could account for this, assuming that laser non-uniformities led to magnetic-field generation centered off of the laser axis.

IV. Estimate of Direct Laser Heating

We turn now to a quantitative analysis of the on-axis aneurisms. The incident laser energy propagates through the underdense ambient medium and deposits the bulk of its energy at the critical surface, which is the target surface at the onset of the laser pulse. Experimental evidence indicates that a burst of UV and X rays are emitted from the target plasma during the laser pulse. This radiation photoionizes the ambient gas (bound-free absorption) and provides the seeds for inverse bremsstrahlung (free-free) absorption of the incident laser beam by the ambient gas. We do not attempt to model this initial target heating and photoionization process here, but instead simply assume that the ambient gas is initially ionized with an ionization fraction that falls as $1/r^2$ where r is the distance from the target. The degree of ionization is found experimentally to be in the range of one to a few percent at a distance of 1 cm from the target.

The formula for the inverse bremsstrahlung absorption coefficient in plasma has been given by Johnston and Dawson.[10] For the present case (electron density much less than critical), this coefficient is:

$$K = \frac{K_b \, \zeta^2 \, \zeta' \, \rho^2 \, \lambda^2 \, \ln\Lambda}{A^2 \, T^{3/2}} \qquad (1)$$

where λ is the laser wavelength, $\ln \Lambda$ is the Coulomb logarithm (varies from 1 - 5 for these cases), ζ is the number of free electrons per ion, $\zeta' = \max(\zeta, 1)$, A is the atomic number of the ions, ρ the mass density of the plasma, and T the local electron

9

temperature. The constant K_b is 1.5666×10^{18} m^{-1} for mks units with T in eV. The important point here is that the absorption depends strongly on ionization state and temperature. The ζ' factor accounts for the presence of neutral ambient atoms at low degrees of ionization.

The time derivative of temperature at a point in the channel is given by:

$$\frac{dT}{dt} = \frac{K\ I}{\rho\ C_v} \qquad (2)$$

where K is given by Eq. (1), I is the local laser intensity, and C_v is the specific heat at constant volume. The intensity will depend on the time variation of the laser as well as the distance from the target. For a perfect gas, $C_v = 1.44 \times 10^8\ (1 + \zeta)/A$ J/eV-kg.

We may integrate Eq. (2) directly to obtain an estimate of the final temperature of the laser-heated channel. We assume fully ionized nitrogen as the ambient gas, ρ for 5 Torr N_2, $\lambda = $ 1 micron, ln $\Lambda = 3$, and find

$$T_f \approx (6\ E/r^2)^{2/5} \qquad (3)$$

where E is the laser energy in Joules, r is the local channel radius in centimeters, T_f the final temperature in eV, and we have assumed that the initial channel temperature is small. Taking $E_1 = 100$ J, and $r = 0.05$ cm, we find $T_f = 142$ eV, so a hot channel is expected and should extend a considerable distance

along the laser channel, since the dependence on distance is weak. The asumptions made to obtain this estimate will be justified later in this paper.

A better estimate of the channel temperature as a function of time (during the laser pulse) and distance from the target is obtained by numerical integration of Eq. (2) with time dependent quantities included. For this estimate, a Gaussian pulse shape is used for the laser power, peaking at 4 ns, ending at 8 ns. The position in the channel determines the level of preionization and the channel radius. The Coulomb logarithm is computed, and ζ is given by a fit to Saha equilibrium at 5 Torr pressure of atomic nitrogen shown in Fig. 5. At this pressure, nitrogen begins to ionize at about 1 eV, is 5 times ionized at 10 - 30 eV, and is fully ionized at 90 eV. The specific heat, Cv, is taken to be the perfect gas value, with a correction term added between 0.1 and 100 eV to model the ionization energy. This term is a linear ramp in log T starting at zero at T = 0.1 eV and climbing to 3×10^8 at T = 100 eV.

We have integrated Eq. (2) for target distances ranging from 0.1 to 3 cm. We call the result of these integrations the "zero dimensional" (or 0-D) model, since each point in the channel is heated completely independently of all other points. The results depend on the degree of preionization of the channel. Fig. 6 shows the case of 5% ionized at 1 cm from the target. Temperatures are shown as a function of distance along the

channel for times of 0 (room temperature) to 8 ns (end of laser pulse). The result from Eq. (3) is labeled "simple model." As expected, Eq. (3) is a good estimate of channel heating for regions that become fully ionized (0 - 0.5 cm), but beyond 0.5 cm the temperature in the channel drops, with little heating beyond 0.9 cm. An ionization front moves to larger radii in this figure with a mean velocity of about 10^8 cm/s, heating the gas from ambient temperatures to about 100 eV, but it is not a progressive wave, since no coupling between different radii is included in the model.

The result is a channel heated to about 100 eV extending from the target to about 1.0 cm along the channel. This heated region expands hydrodynamically as a cylindrical shock wave and forms a low density channel at later times. The spherical blast wave expands more rapidly in this channel, resulting in aneurism formation. When the blast wave moves beyond the heated region, the aneurism should decay.

The length of the heated region, L_n, depends on the laser energy, the degree of preionization of the ambient gas, and on the pressure of the ambient gas. The 0-D model results are fit to an accuracy of 2% by the scaling law:

$$L_n \text{ (cm)} = 0.19 \, E^{0.16} \, P^{0.16} \, \zeta_0^{0.33} \qquad (4)$$

where P is the ambient pressure of N_2 and ζ_0 is the percent preioniztion at 1 cm from the target. For example, for $\zeta_0 = 1\%$, $E_1 = 109$ J, and P = 5 Torr, we find $L_n = 0.52$ cm. The energy

scaling of Eq. (4) is that of a normal blast-wave (see Eq. (5), below), but the pressure scaling is exactly the opposite of the blast-wave case. This means that, as the ambient pressure is increased, the size of the aneurism produced increases while the position of the blast wave decreases, causing the pressure dependence to be the most obvious in the experiments.

This model makes no allowance for a variety of possible cooling mechanisms, and thus represents an upper limit estimate of the channel heating. We will show in the next Section, however, that the 0-dimensional results agree quite well with detailed 2-dimensional models where all of the important physics has been included.

V. Two Dimensional Simulations of On-Axis Aneurisms

A. Two-Dimensional Code

We have performed 2 1/2-dimensional computer simulations of the NRL laser-target-ambient system with MACH2, an MHD code described in detail elsewhere.[11] The code is axisymmetric with the axis of symmetry appearing as a vertical line to the left in computer-generated pictures. Rotational symmetry about this axis is assumed. The simulations discussed herein take place on numerically generated Eulerian meshes, one of which is illustrated in Fig. 7. The difference equations are of the finite volume type which is well suited to non-rectangular meshes required for problems with complex shapes. Tabular equations of state are used for each distinct material modeled in a

simulation. Our numerical models include the effects of thermal conduction with a thermal conductivity proportional to $T^{5/2}$. Although, these models do not include the effects of thermally generated magentic fields,[9] we have found that such fields do not affect the behavior of the blast front and aneurism discussed here.[12]

B. Results of Two-Dimensional Simulations

The analysis in Sec. IV suggests that laser energy, sufficient to raise the temperature in a long narrow channel on the order of 100 eV, is absorbed by the ambient plasma if we assume that a few percent of the atoms in that medium are singly ionized at a distance 1 cm from the target. Recall that our model for preionization descreases with the square of the distance from that focal spot. MACH2 simulations were performed with a variety of values for the preionization. When the ambient medium is not preionized, there is no laser-induced channel and the blast wave is spherically symmetric -- there is no aneurism. Non-zero values that were used include 0.25%, 1%, 3%, 5%, 10%, and 30%. MACH2 results for the case of 5% initial ionization 1 cm from the target compare most favorably with experimental data, and this is the value used in the simulations discussed below. By varying the degree of preionization in MACH2 simulations, we have found that a heated channel that extends well beyond the blast front at early times is the progenitor of the aneurism that is seen at late times.

Results from MACH2 calculations of a focused laser pulse interacting with a solid aluminum target in a 5 Torr partially ionized gas (80% nitrogen, 20% oxygen), both initially at room temperature, are illustrated in Fig. 8. This is a simulation of the NRL experiment from which the dual-time shadowgram, Fig. 2A, was taken. The laser spot radius is 100 microns on the aluminum target. In Fig. 8, we plot the temperature through a slice down the laser channel on a log scale as a function of distance from the laser focal spot at 1 ns intervals between the times of 1 and 8 ns from the beginning of the laser pulse. The pulse shape is the same as described earlier -- peaking at 4 ns and ending at 8 ns -- depositing 109 J into the target and the ambient medium. The temperature reaches a maximum of approximately 1 KeV at the laser focal spot where the density is greater than the critical density for 1 micron light and the peak laser intensity is 7 x 10^{13} Watt/cm^2. In the heated channel, the ambient medium is heated rapidly (1 ns) to temperatures exceeding 1 eV near the target. At the end of the laser pulse at 8 ns, the channel has been heated to about 100 eV to a distance of 9 mm, and to about 1 eV at larger distances. Fig. 8 may be compared directly to the results of the 0-D model shown in Fig. 6. Aside from the hot target, the two models agree almost exactly, showing that direct inverse Bresstrahlung deposition is responsible for the heating.

Energy absorbed by the narrow laser channel induces a weak cylindrical shock as the heated material flows radially outward. The material in the laser-heated channel expands from the

laser-axis into the cold ambient medium outside the laser beam. Consider a particular location some distance from the target surface. If the density at that axial location in the channel falls below the ambient value before debris from the laser-ablated target reaches that location, the debris will advance more rapidly in the axial direction within the semi-evacuated laser channel. The resulting decline of the density within the channel and outside the blast front is illustrated in Fig. 9, where the log of the density is plotted against the distance from the laser focal spot down the same slice of the channel as was chosen for Fig. 8. In order to resolve the narrow blast front, Fig. 9 is drawn on a finer scale that Fig. 8. The blast front is a well-defined shell in which the density changes by a factor of 9 over a 0.25 mm distance at 8 ns. The density in the channel ahead of the blast front is between 1/3 and 1/6 the ambient value of 8.2 x 10^{-6} gm/cc. The center of the shell is located 2.5 mm from the laser focal spot at 8 ns. The heated channel, however, extends well beyond the shell out to 9 mm from the focal spot by the end of the laser pulse. This distance is, as shall see, sufficient to allow an aneurism to form. The portion of the shell that travels within the low-density channel moves ahead of the portion that travels through the relatively more dense non-heated ambient gas. Without increasing the total laser energy, a hotter channel, and hence a stronger cylindrical shock, is obtained with a larger initial fractional ionization of the ambient medium.

Early time development of the laser-induced channel and its interaction with the blast from the target is shown in Fig. 10. The dimensions of this mesh are 5 mm x 2.5 mm, with 64 computational cells in the axial direction and 20 cells in the radial direction, 4 across the laser beam. Contours of constant electron number density and plasma velocity vectors are illustrated in the region close to the target on this grid at 4, 7, and 10 ns after the beginning of the laser pulse. One can clearly see the formation of the laser-heated channel outside the expanding blast front, and a jet of plasma from the blast front expanding faster within the channel than without. The aluminum/air interface is noted by a dashed line on the number density contour plots. The temperature near this interface is 120 eV at 4ns, 330 eV at 7 ns, and 170 eV at 10 ns. The calculated temperature within the cylindrical shock is 7 eV at 4ns, 6 eV at 7 ns, and 2 eV at 10 ns. The peak velocities at these times are between 5×10^7 cm/sec and 6×10^7 cm/sec. By 10 ns, a jet of aluminum target materials is evident, propagating within the channel ahead of that in the surrounding blast front.

Fig. 11 illustrates the state of a simulation performed on a large grid (1.5 x 0.75 cm) with 64 axial and 20 radial cells at 10, 30, and 71 ns. We again show contour plots of the electron number density and plasma velocity vectors. At 10 ns, the hot plasma within the channel (where the temperature is above 50 eV) extends 1.0 cm from the target. The expanding bubble is substantially behind at this time -- a distance of 0.3 cm from the target surface. The protrusion on the axis at 10 ns is not

the aneurism, but is the heated channel. The aluminum/air interface within the channel is much closer to the target than the tip of the electron density protusion. The temperature of the shell is on the order of 10 eV at 10 ns and cools to 1 eV by 71 ns. The maximum velocity at 30 ns is 1.2×10^7 cm/sec, and is 8.5×10^6 cm/sec at 71 ns. The complex flow pattern evident at later times is created by interaction of the spherical blast wave emanating from the target with the cylindrical shock. The aneurism itself is clearly defined by 71 ns. The electron number density contours are closely spaced at the location of the shell. It is this shell, the locus of points at which there are large gradients in electron number density, that is to be compared to experimentally produced shadowgrams. The aneurism, while evident at 71 ns in Fig. 11, is not quite as large as that seen in the experiment at 71 ns (Fig. 2a).

We have included effects of radiation cooling, assuming the optically thin limit in the low density plasma, in a similar set of simulations. The general character of the blast front, laser-induced channel, and the resulting aneurism are unchanged. Furthermore, the models discussed above assume the preionization happens instantaneously at the time the laser pulse begins. In reality, the ionization of the ambient medium may not occur instantaneously, so we have performed a simulation in which the degree of preionization is zero initially and ramps linearly with time to a maximum value of 5% at the time of peak laser power. The extent of the laser-induced channel and the size of the aneurism are essentially the same as the case discussed above.

C. Comparison With Experiment

The target plasma/nitrogen plasma interface (outside the laser channel) is in the blast-wave that propagates spherically from a point source according to the similarity relation; $R \propto (E/P)^{1/5} t^{2/5}$. For our present experiment, the motion of the blast-wave is described by[1]

$$R = 0.12 \left(\frac{E}{P}\right)^{1/5} t^{2/5} \qquad (5)$$

where R is in centimeters, energy (E) is in Joules, ambient pressure (P) is in Torr, and time (t) is in ns. For shot #85-544 (Fig. 2a), which had a 109 Joule laser pulse and 5 Torr ambient nitrogen pressure, the radius of the blast front at 71 ns is 1.25 cm. To facilitate a comparison between the MACH2 simulations discussed in Sec. V B and the experiment, we display a digitized plot of the shadowgram from the shot #85-544 in Fig. 12a. In Fig. 12b, we display the contour plot of the electron number density from the simulation with 5% preionization, drawn to the same scale as the shadowgram. The MACH2-simulated location of the debris/air interface outside the laser cone agrees with that of the experiment. Further the location of the debris/air interface in Figs. 12a and 11b is 1.2 cm from the target surface, in agreement with that predicted from the blast-wave model, Eq. (5). The location and size of the central aneurism simulated by MACH2 is remarkably like that produced by the experiment.

We speculate that numerical diffusion in our Eulerian calculations together with the lack of resolution in the laser channel (recall that there are but 4 cells radially across the channel) causes the MACH2 simulated aneurism to be flattended at its tip rather than to protrude as far from the target as the experimentally generated aneurism.

VI. Cylindrical Shocks

We now examine more closely the laser-heated channels which, as our simulations show, lead to the on-axis aneurisms. The localized energy deposition near the axis of the laser beam produces the cylindrical shock or blast-wave that is observed in the early-time shadowgrams. Fig. 13 shows a digitization of the shadowgram of shot #86-625 (solid line), taken 14 nsec after the peak of the laser pulse. The plastic (CH) target was in a 5 Torr ambient of nitrogen. The laser pulse had a width (FWHM) of 3 nsec and delivered 238 Joules; the focal spot incorporated ISI smoothing and had a 500 micron radius. The cylindrical shock can be seen in Figure 11 between 9 and 14 mm from the target. This shot was simulated with MACH2, again assuming five percent preionization 1-cm from the focal spot, and placing 8 computational cells across the laser spot. Fig. 13 also shows (dashed line) a superposition, drawn to the same scale, of the simulated electron number density. The channels seen in the simulation and shadowgram are similar.

The laser energy deposition, being of short duration (3 nsec) and localized near the laser axis, suggests that the cylindrical shocks could be represented by a cylindrical blast-wave model. At the top of Fig. 14 is plotted, from several of the early-time shadowgrams, the cylindrical radius versus the axial position from the target. From this, a plot is made at the bottom, for the fixed axial position of 1.4 cm, of cylindrical radius versus the square root of time. This is the theoretical time dependence of an ideal cylindrical blast-wave. The coefficient which fits the data implies an energy deposition per unit length of about 1.8 J/cm at R=1.4 cm. More energy per unit length is deposited nearer the target and less further away. The simulation, on the other hand, shows somewhat less energy (1.0 J) in the channel. The small discrepancy could be due to violation of the blast-wave model assumption, the simulation or both. For example, the blast-wave model assumes an instantaneous energy deposition. Due to the finite duration of the laser pulse, the expansion during the laser pulse may be closer to a detonation wave. On the other hand, the simulation results are dependent upon the assumptions of the ionization model and the treatment of thermal transport. For example, our model does not currently include the effects of thermally-generated magnetic fields or radiation transport.

VII. Conclusion

We have presented data supporting a laser-heated channel mechanism for on-axis aneurism production. These aneurisms can be explained by the laser heating of a low-density channel along the laser axis. The 2-D simulation based on the channel mechanism give good agreement with the observed aneurisms.

References

1. B.H. Ripin, A.W. Ali, H.R. Griem, J. Grun, S.T. Kacenjar, C.K. Manka, E.A. McLean, A.N. Mostovych, S.P. Obenschain, and J.A. Stamper in Laser Interaction and Related Plasma Phenomena, Vol 7, Edited by H. Hora and G. Miley (Plenum. New York, 1986), p. 857.

2. Actually, theoretical treatments of the hydrodynamic instability of blast waves have been somewhat controversial. However, instability has not been shown in a definitive experiment. Some theoretical treatments on the subject include: H. Murakami, T. Yabe, and K. Niu, Trans. Japan Soc. Aero. Space Sci. 20, 100 (1977); B. Gaffet Ap. J. 279, 419 (1984); A. Cheng, Ap. J. 227, 955 (1979); S.I. Anisimov and Ya. B. Zeldovich, Sov. Tech. Phys. Lett. 3, 445 (1977) (Eng. Trans.); and I.B. Bernstein and D.L. Book, Ap. J. 240, 223 (1980).

3. J. Grun, R. Stellingwerf, B.H. Ripin, Phys. Fluids 29, 10 (1986).

4. J.A. Stamper, E.A. McLean, S.P. Obenschain, and B.H. Ripin, in Fast Electrical and Optical Measurements, Vol. II-Optical Measurements, edited by J. E. Thompson and L.H. Leussen Martinas Nijoff, Dordrecht, 1986), p. 691.

5. R.H. Lehmberg and S.P. Obenschain, Opt. Commun. 46, 27 (1983).

6. J.G. Lyon, NRL Memo Report 5491 (1985), NTIS No. ADA154915; R.E. Peterkin, Jr., R.F. Stellingwerf, B.H. Ripin, and J.A. Stamper, Bull. Am. Phys. Soc. 31, 1585 (1986).

7. C. Longmire, private communication.

8. J.L. Giuliani, Jr., NRL Memo Report 5420 (1984), NTIS No. ADA147006.

9. J.A. Stamper, NRL Memo Report 3872 (1978). NTIS No. ADA061944. See also chapter on spontaneous magnetic fields by J.A. Stamper in Handbook of Plasma Physics, Volume on Physics of Laser-Plasma, edited by S. Witkowski and A. Rubenchik (North Holland, Amsterdam), to be published, 1988.

10. T.W. Johnston and J.M. Dawson, Phys. Fluids, 16 722 (1973).

11. M.H. Frese, "MACH2: A Two-Dimensional Magnetohydrodynamical Simulation Code for Complex Experimental Configurations," AMRC-R-874,1987.

12. R.E. Peterkin, Jr. and R.F. Stellingwerf, Bull. Am. Phys. Soc., 32, 1909 (1987).
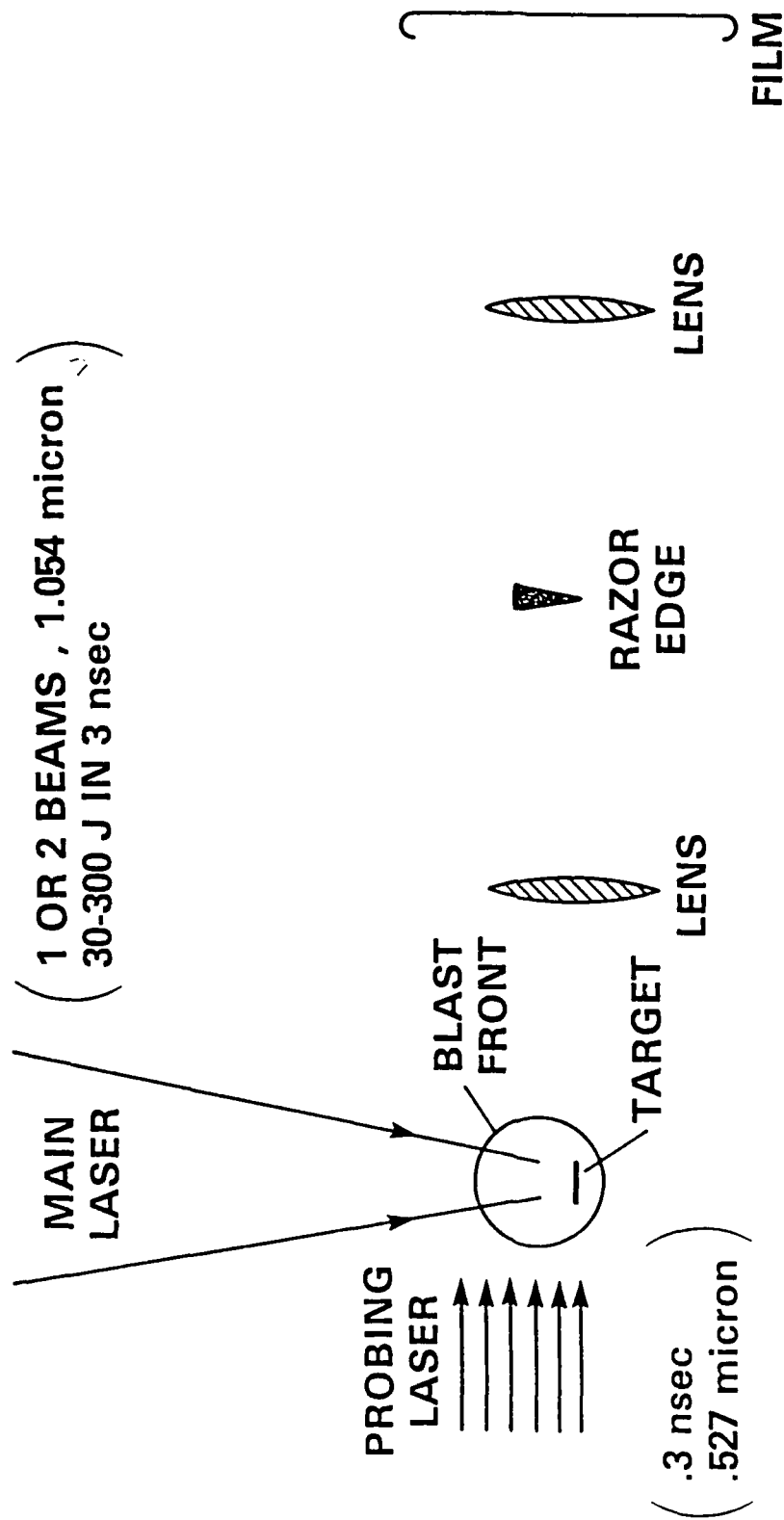
Fig. 1.   Experimental arrangement for dark-field shadowgraphy.
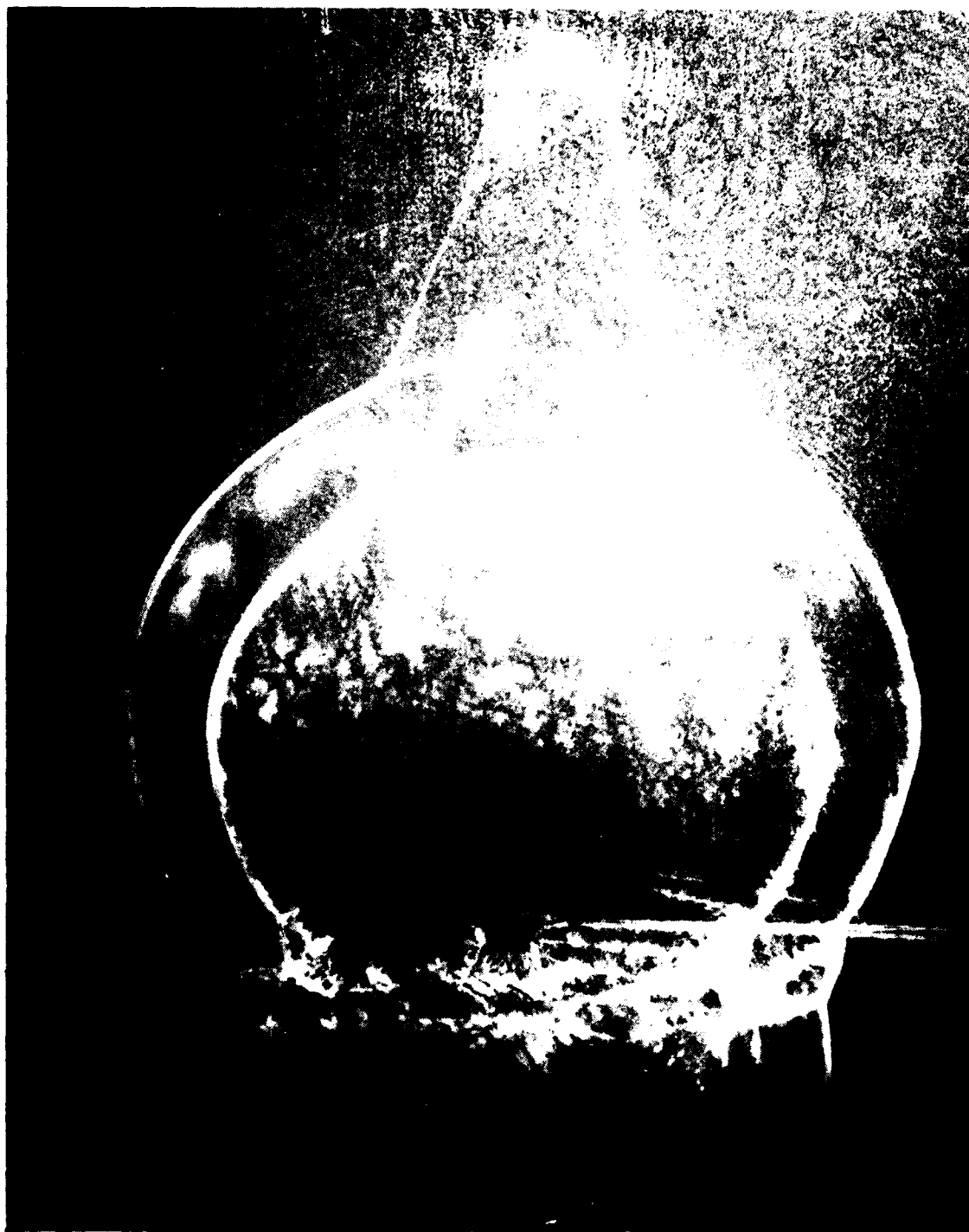
(a) Dark-field shadowgram of shot #85-544 (109 v; 5 T, N_2) showing on-axis aneurism growth at times 71 and 146 nsec. A 1-cm size marker is shown on the right.

Fig. 2 — Dark-field shadowgrams of on-axis aneurisms

(b) Early-time (16 nsec) dark-field shadowgram of shot #86-624 (245 J; 5 T, N_2) showing a cylindrical shock propagating away from the laser axis.

Fig. 2 (Continued) — Dark-field shadowgrams of on-axis aneurisms

(a) Dark-field shadowgram of a 30-degree tilted target for shot #86-581 (95 J; 5 T, N₂) showing on-axis aneurism at 59 nsec. A 1-cm size marker is shown on the left.

Fig. 3 — Dark-field shadowgrams showing aneurism formation using tilted targets.

28
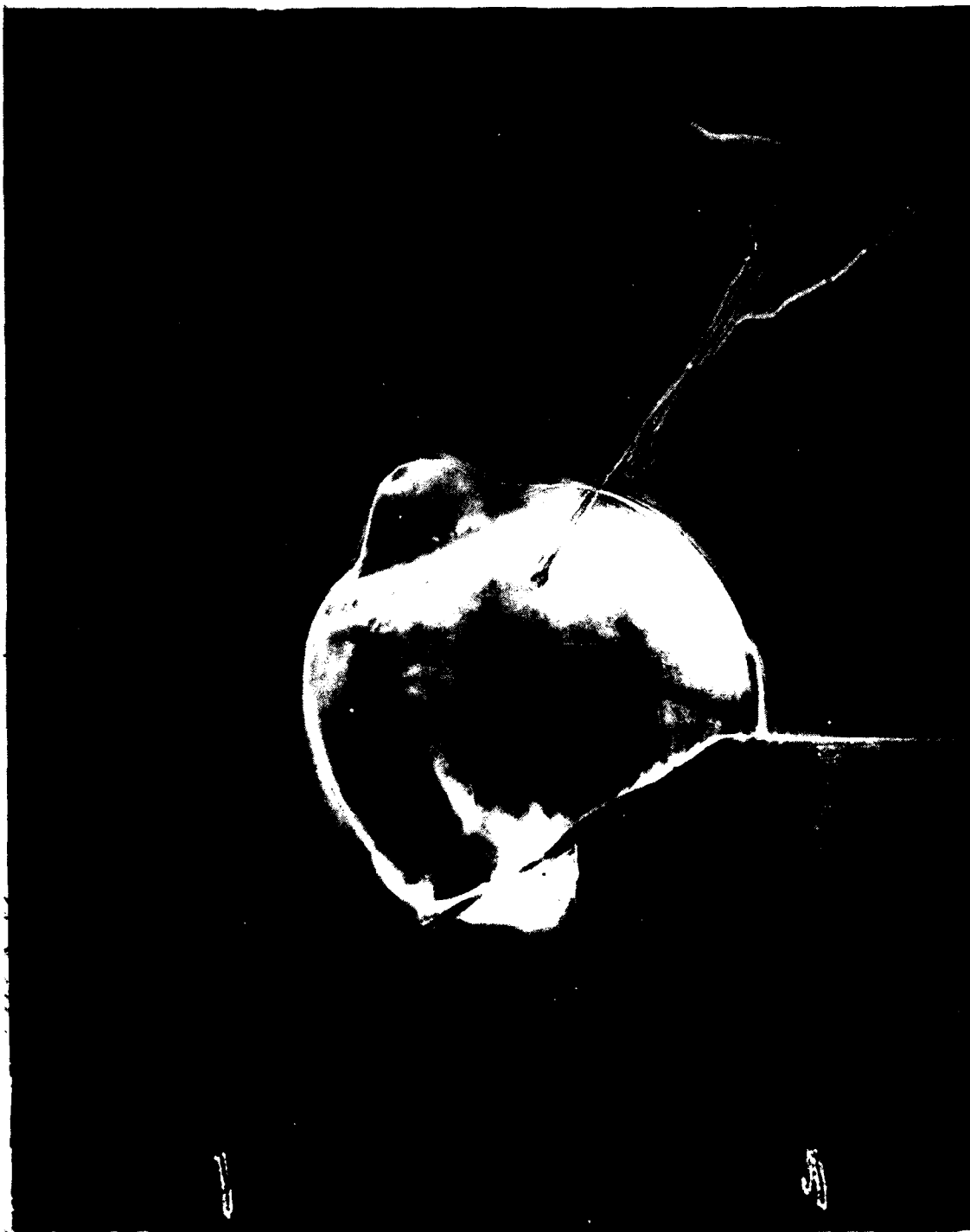
(b) Dark-field shadowgram of a 30-degree tilted target for shot #86-583 (3.6 J; 5 T, N_2) showing aneurism along the target normal.

Fig. 3 (Continued) — Dark-field shadowgrams showing aneurism formation using tilted targets.

Fig. 4 — Low-energy (4.1 J), 5 T N₂ shot dark-field shadowgram, showing multiple aneurisms or front break-up at 52 and 96 nsec.
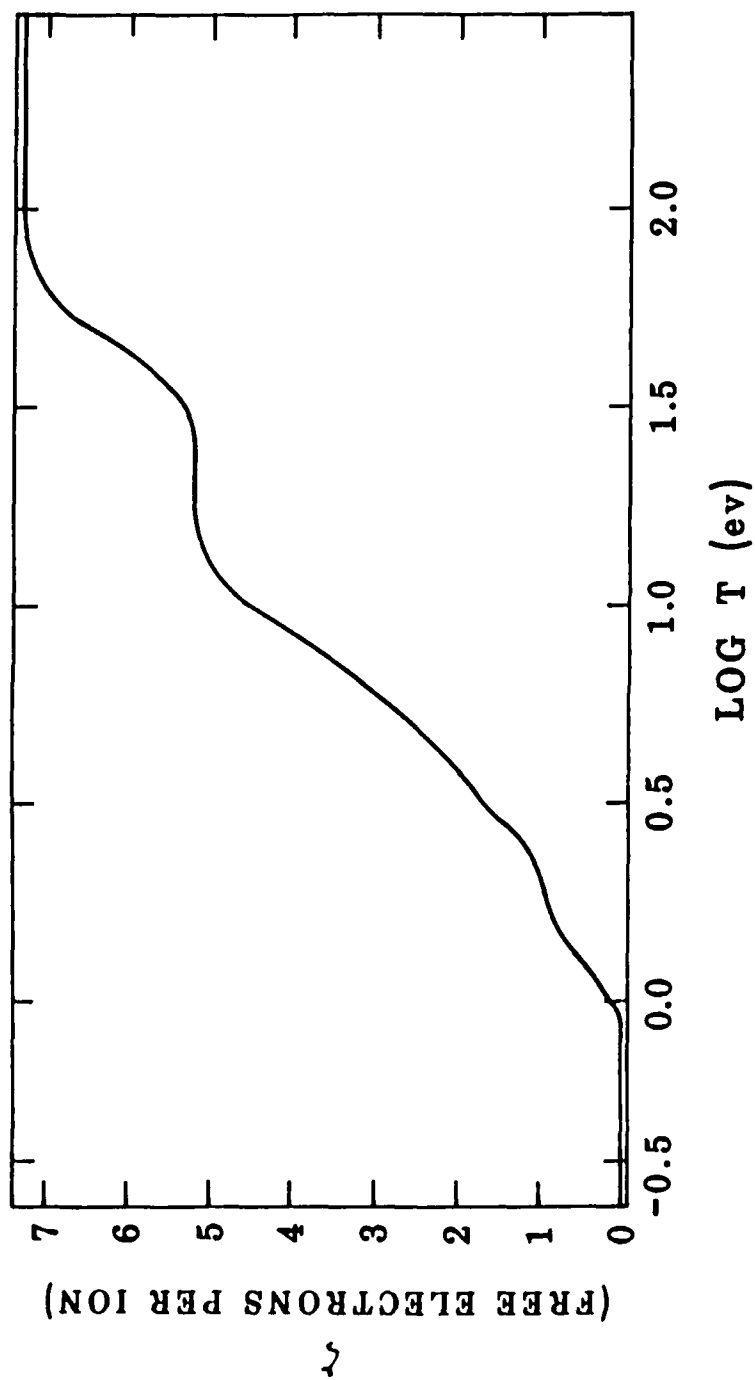
Fig. 5. Ionization state as a function of Temperature for 8.2 10⁻⁵ gm/cc (approximately 5 Torr) Dry Air (from SESAME EOS tables at LANL).
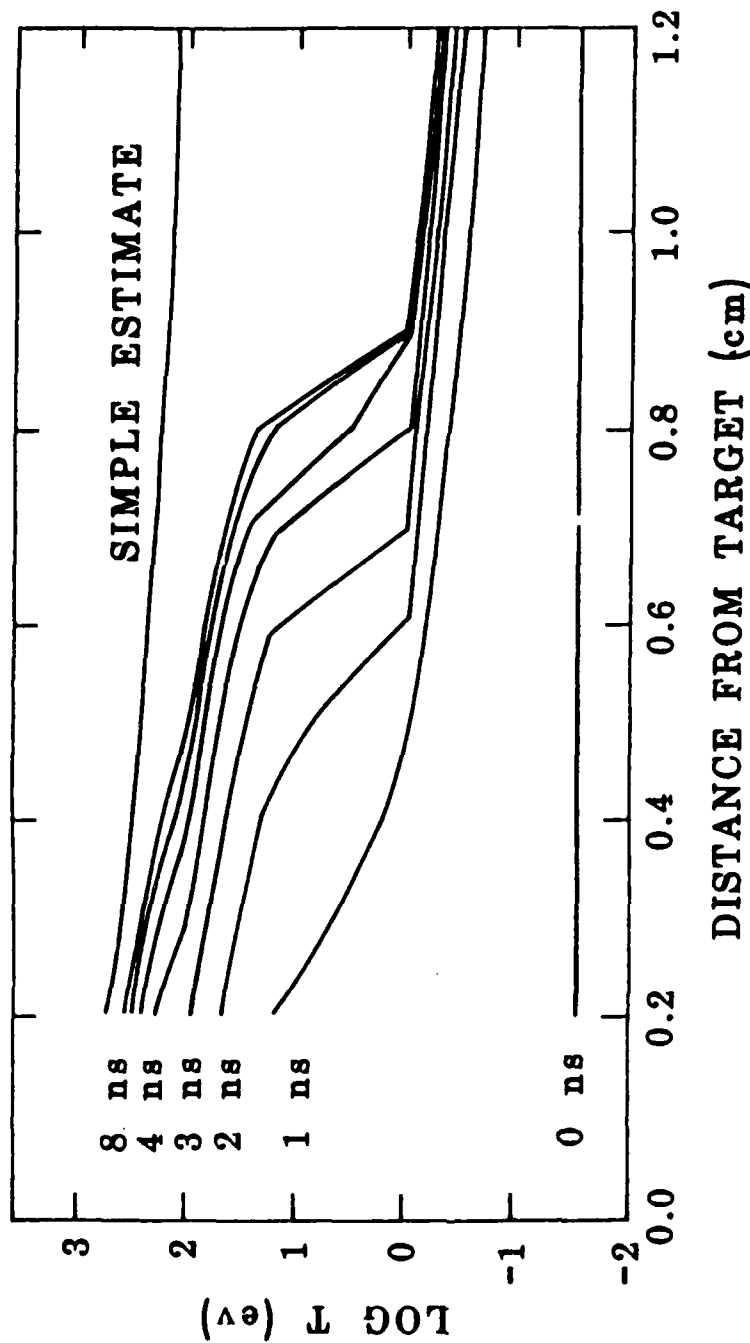
Fig. 6. Log temperature versus distance from laser focal spot for the analytic and 0-D models of a 5% preionized 5 Torr plasma at 1 ns intervals during the laser pulse.
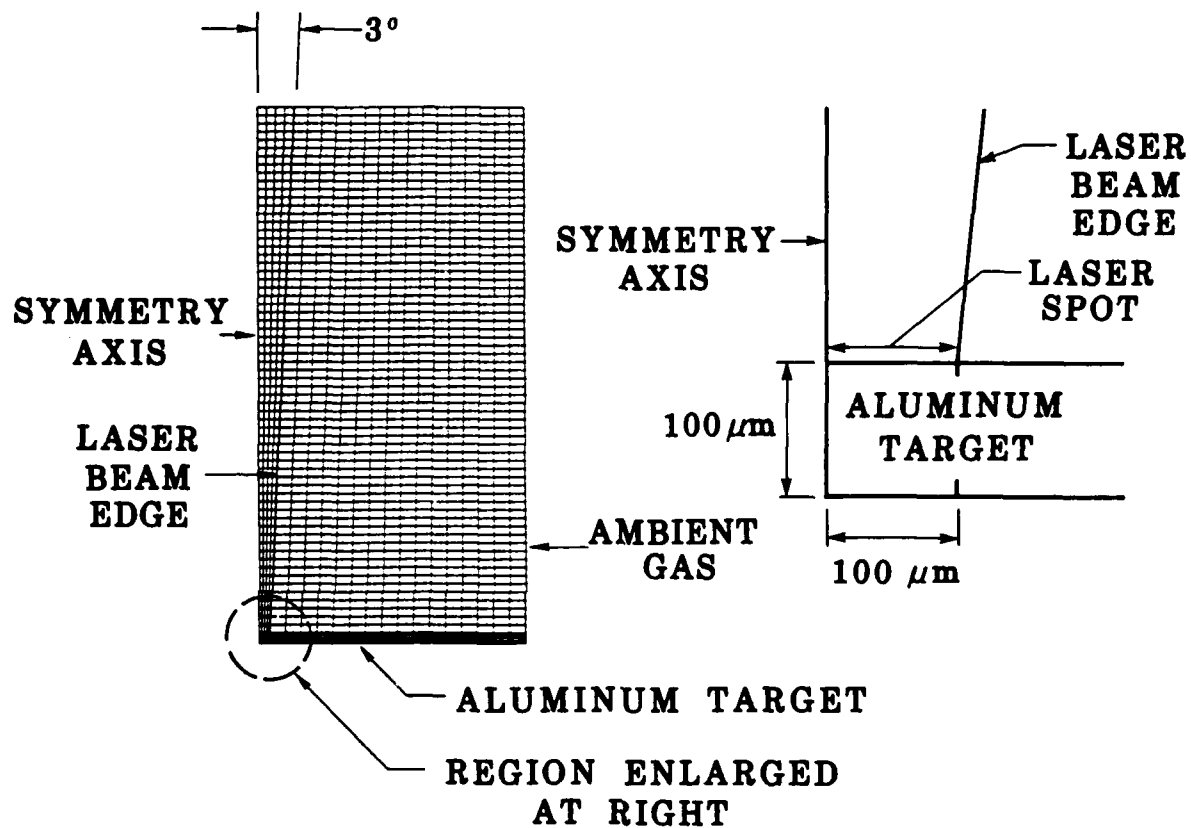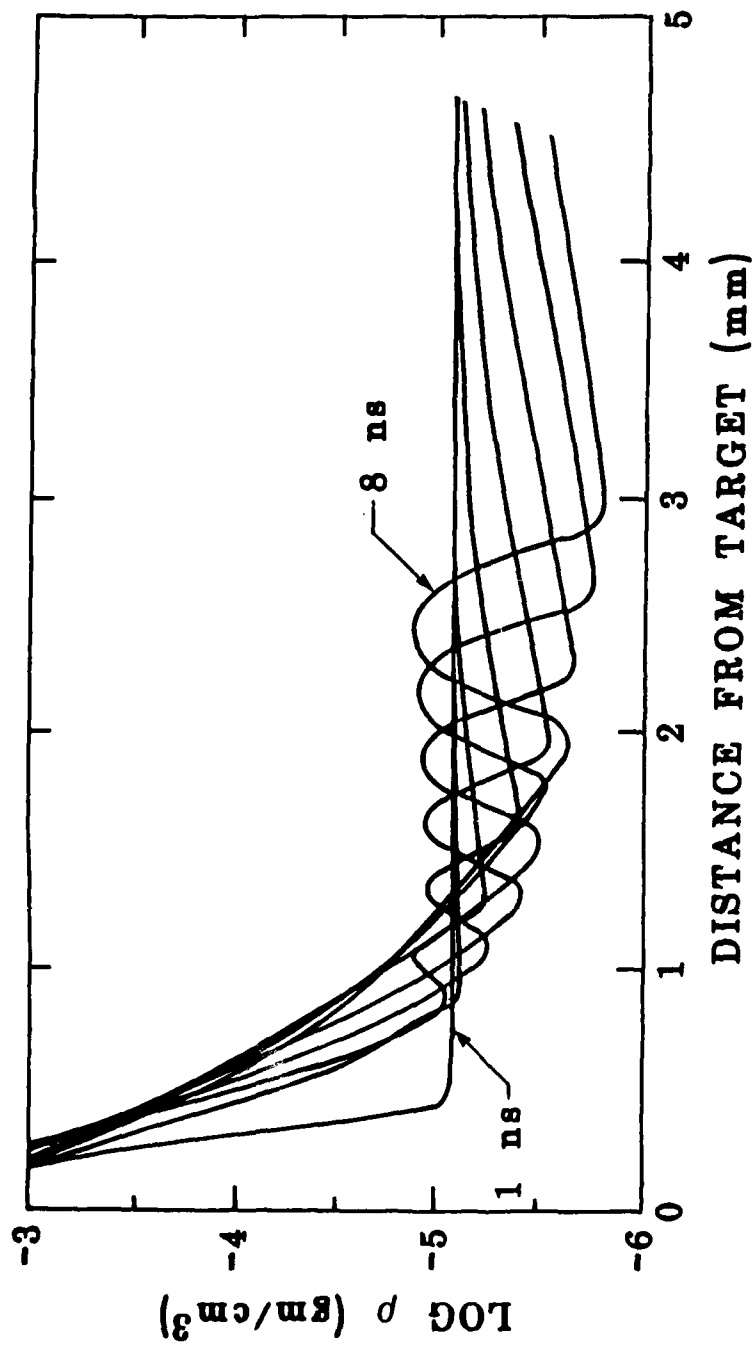
Fig. 7.   Outline of the calculation mesh for MACH2 simulations.
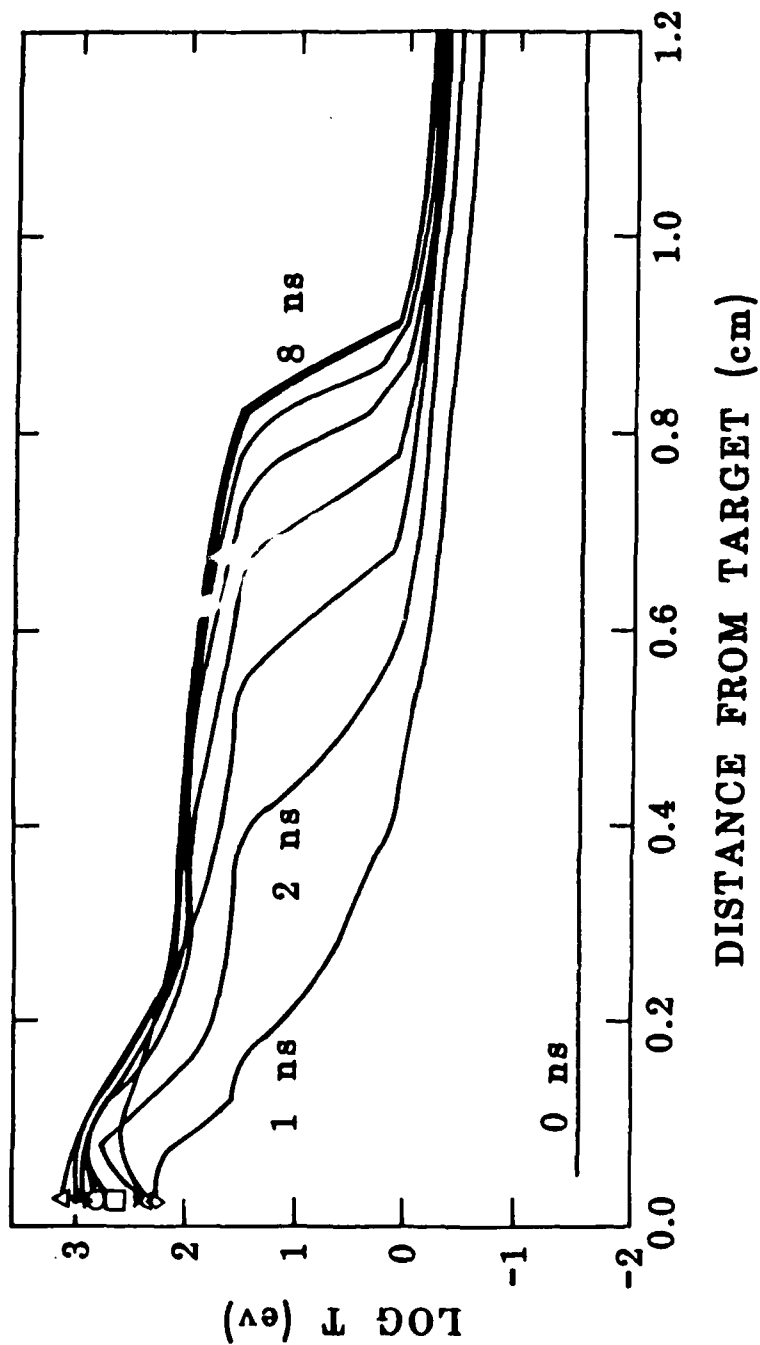
Fig. 8. Log temperature versus distance from laser focal spot for a MACH2 simulation of a 5% preionized 5 Torr plasma at 1 ns intervals during the laser pulse.

Fig. 9. Log density versus distance from laser focal spot for
a MACH2 simulation of a 5% preionized 5 Torr plasma at 1 ns
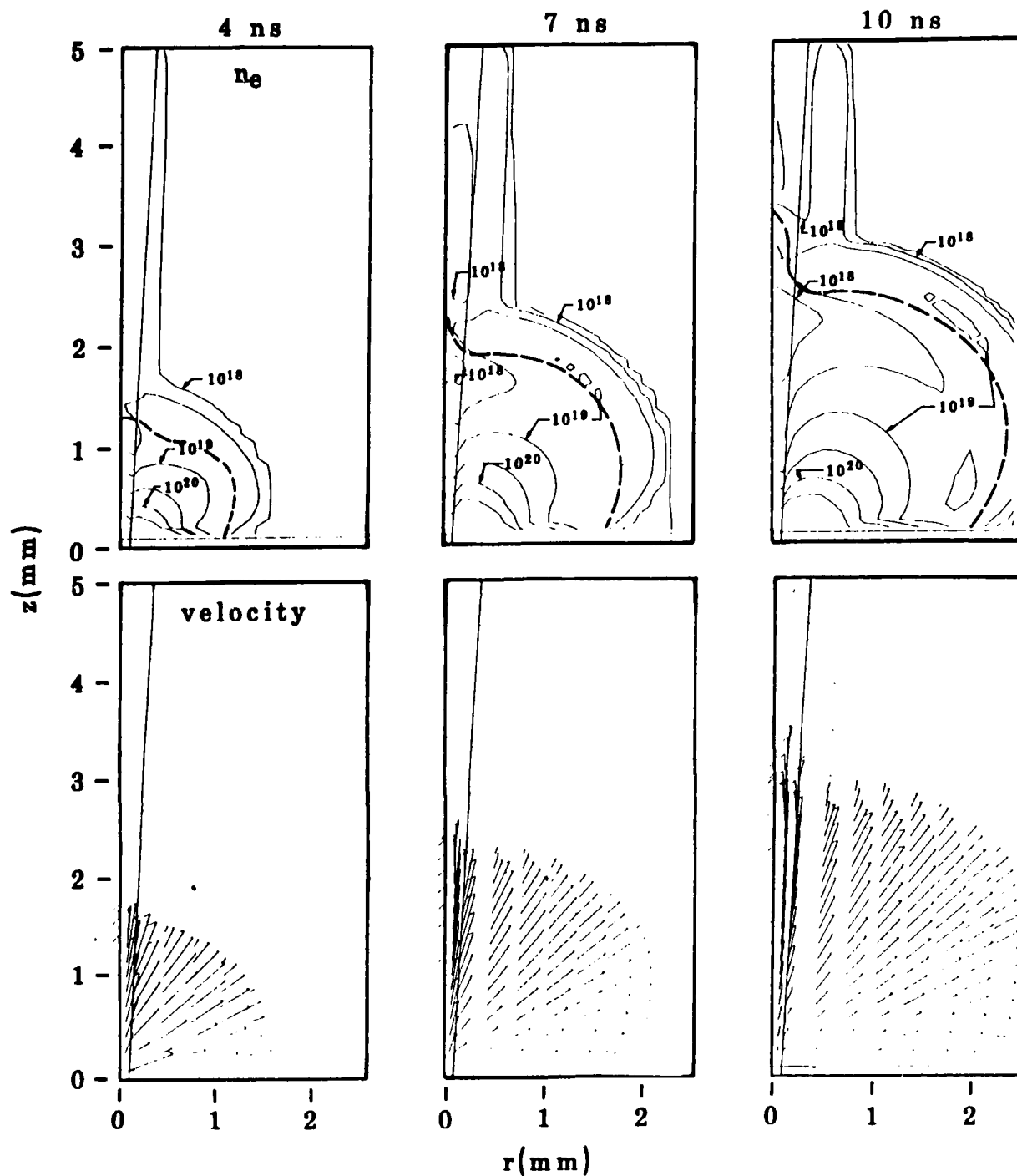intervals during the laser pulse.

Fig. 10. Electron number density contours (above) and velocity
vectors at 4, 7, and 10 ns on a small computational mesh.
The contour levels (electrons/cm³) are equally spaced on a
logarithmic scale. The dashed line is the location of the
aluminum/air interface. The laser-heated low-density channel
extends well beyond the spherical blast wave at 10 ns, and
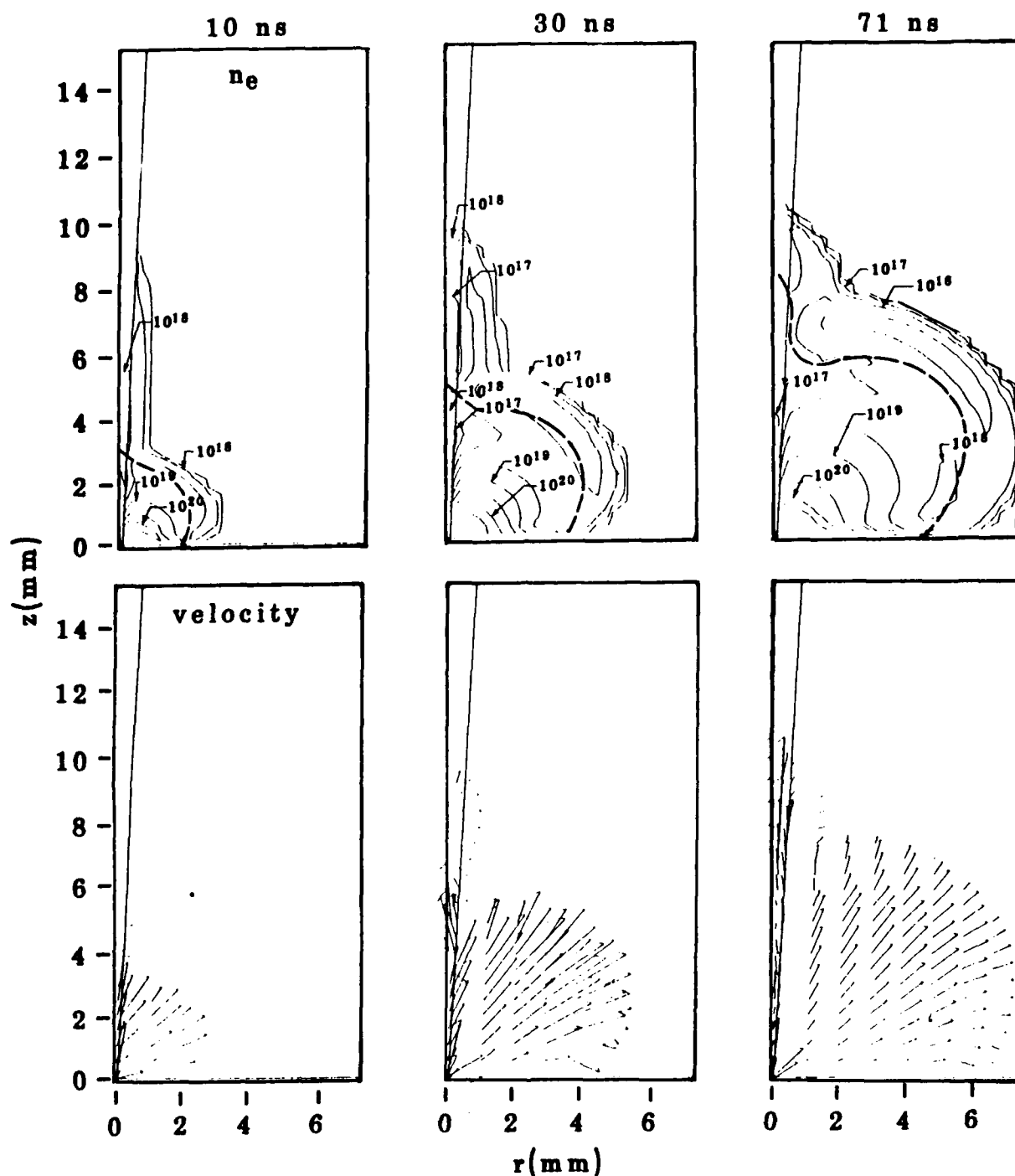this allows the aneurism to form.

36

Fig. 11. Electron number density contours (above) and velocity vectors
at 10, 30, and 71 ns on a large computational mesh. The
contour levels (electrons/cm^3) are equally spaced on a
logarithmic scale. The dashed line is the location of the
aluminum/air interface. The laser-heated low-density
channel extends well beyond the spherical blast wave at 10
ns, and this is the aneurism at late times.
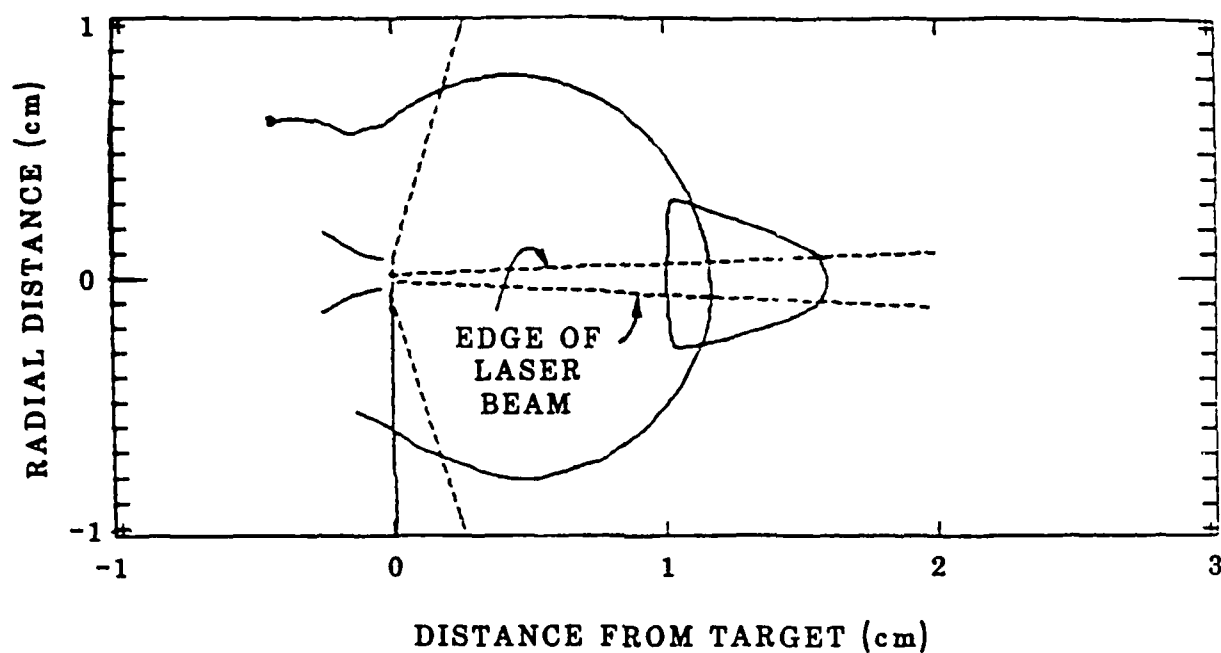
a. Digitzation of shadowgram showing shell and aneurism at 71 ns.
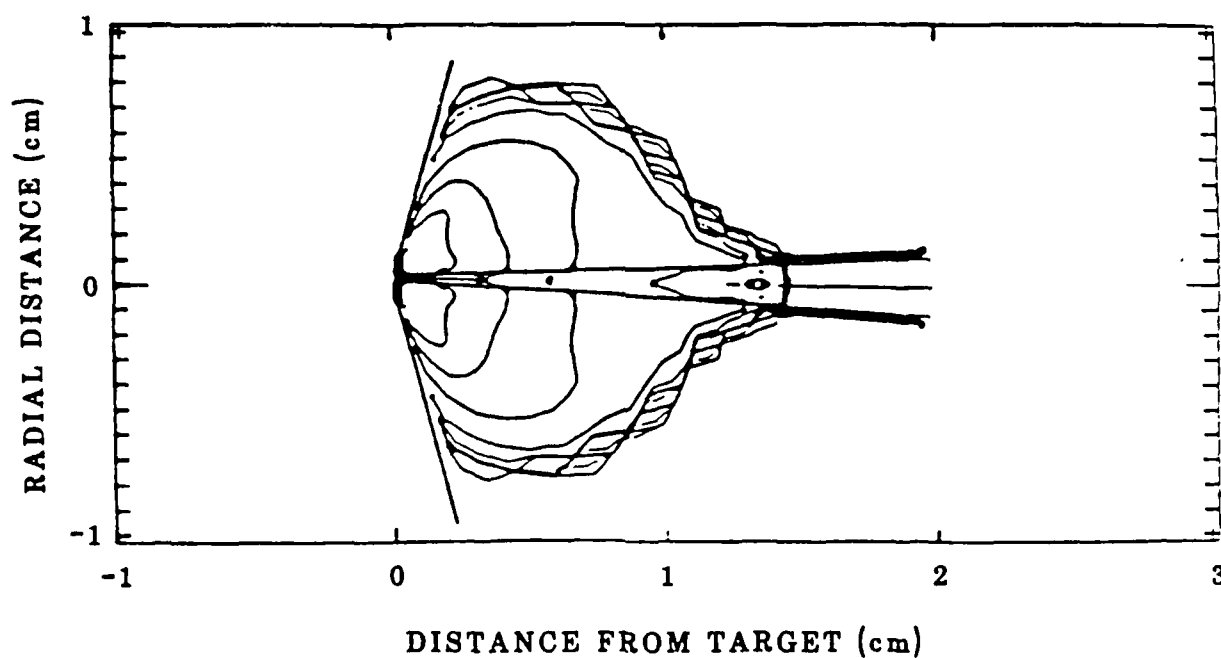
b. Contour plot of electron number density at 71 ns for the MACH2 simulation.

Fig. 12. Comparison of experimental aneurism and simulation for shot #85-544.
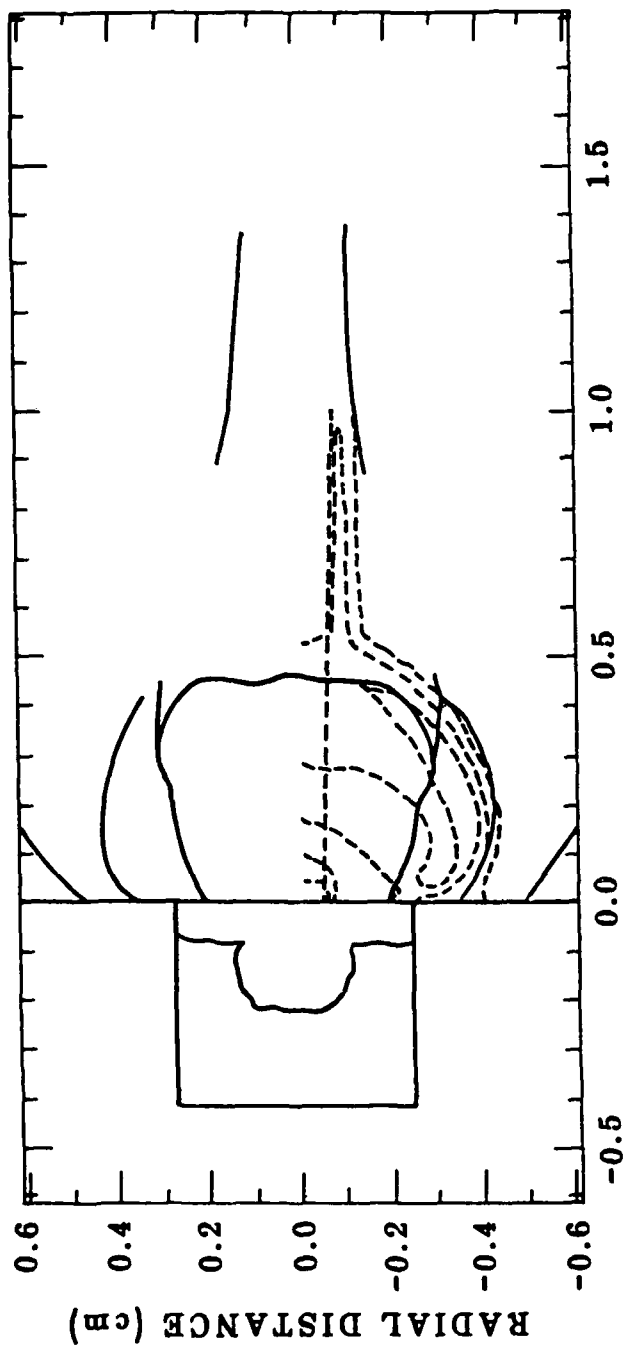
Fig. 13. Cylindrical shock formation at early time (14 ns) in shot #86-625. The solid lines are a digitization of the shadowgram and the dashed lines (lower half) are the electron number density contours from a MACH2 simulation of this shot.
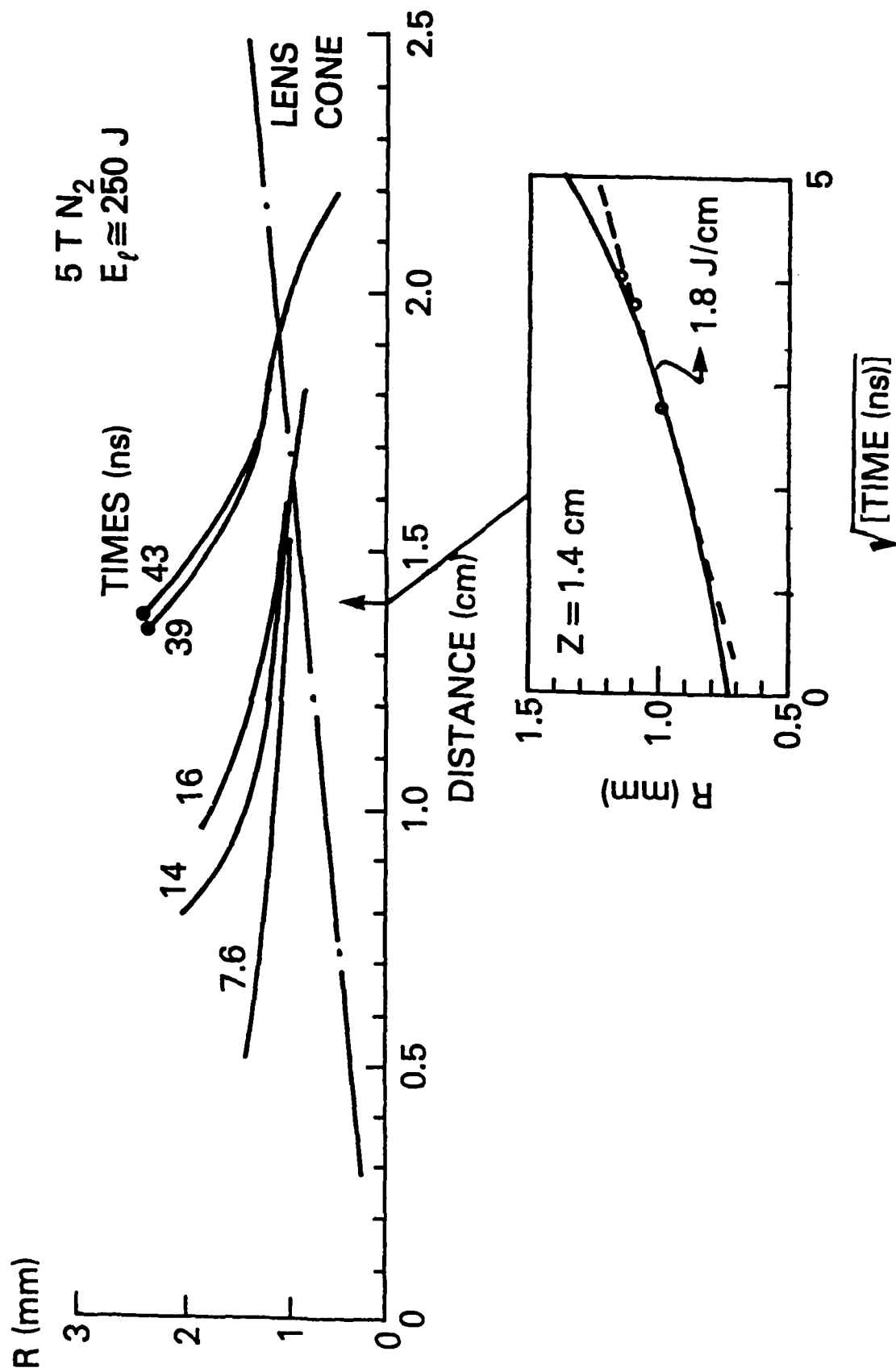
Fig. 14.   Comparison of experimental shock motion from the laser
channel with a cylindrical blast-wave model.

40

DNA DISTRIBUTION LIST FOR REPORTS

AIR FORCE GEOPHYSICAL LAB.
Infrared Tech. Div. - LSI
Hanscom AFB, MA 01731
    H. Gardiner

AUSTIN RESEARCH ASSOCIATES
1901 Rutland Avenue
Austin, TX 78758
    R. Thompson

BERKELEY RESEARCH ASSOCIATES
P.O. Box 241
Berkeley, CA 94701
    S. Brecht
    C. Prettie
    J. Workman
    V. Thomas

CORNELL UNIVERSITY
Plasma Studies
309 Upson Hall
Cornell University
Ithaca, NY
    D. Hammer

DEFENSE NUCLEAR AGENCY
Washington, D.C. 20305
    Ms. J. Pierre
    Dr. B. Prasad
    Dr. K. Schwartz
    Dr. G.W. Ullrick
    Dr. T. Walsh
    Dr. L.A. Wittwer
    Dr. M. Owais

EOS TECHNOLOGIES INC.
606 Wilshire Blvd., Ste. 700
Santa Monica, CA 90407
    B. Gabbard
    R. LeLevier

FLUID SCIENCES
5871 Aylesboro Road
Pittsburg, PA 15217
    N. Zabusky

JAYCOR
P.O. Box 85154
San Diego, CA 92138
    J. Sperling
    N. Krall

LOS ALAMOS NATIONAL LAB.
Los Alamos, NM 87545
    J. Borovsky
    S.P. Gary
    P. Kadish
    M. Pongratz
    D. Sappenfield
    G. Smith
    D. Winske

MAXWELL - 8-Cubed Division
1800 Diagonal Road
Alexandria, VA 22314
    K. Hain

MISSION RESEARCH CORPORATION
1720 Randolph Road, SE
Albuquerque, NM 87106
    R. Peterkin
    R. Stellingwerf
    L. Sloan

MISSION RESEARCH CORPORATION
Drawer 719
Santa Barbara, CA 93102-0719
    R. Bigoni
    G. Bullock
    F. Fajen
    R. Goldflam
    A. Gregersen
    M. Hansman
    R. Kilb
    D. Landman
    C. Longmire
    D. Maloof
    T. Mazurek
    P. Ricchiazzi
    D. Sowle
    T. Old
    W. White
    E. Witt

MISSION RESEARCH CORPORATION
One Tara Blvd., Ste. 302
Nashua, NH 03062
    R. Armstrong

NAVAL RESEARCH LABORATORY
Code
4700 W. Ali
4780 J. Fedder
4780 J. Giuliani
4732 H. Griem
4732 J. Grun
4780 J. Huba
4732 K. Kearney
4786 M. Keskinen
4732 T.N. Lee
4780 J. Lyon
4732 C. Manka
4732 E. McLean
4732 - A. Mostovych
4780 M. Mulbrandon
4731 S. Obenschain
4700 S. Ossakow (26 cys.)
4732 C. Pawley
4732 T. Peyser
4732 B. Ripin (50 cys.)
4732 J. Stamper
4780 S. Zalesak

PLASMA RESEARCH CORPORATION
5850 Leesburg Pike #23
Falls Church, VA 22041
    J. Guillory

2990 Main Street
Alameda, CA 94501
    G. Dahlbacka

PHYSICAL RESEARCH, INC.
P.O. Box 30129
Santa Barbara, CA 93131
    J.H. Thompson

PHYSICAL RESEARCH, INC.
134 Holiday Court, Ste. 309
Annapolis, MD 21401
    H.C. Fitz

R&D ASSOCIATES
P.O. Box 9695
Marina Del Rey, CA 90295-2095
    L. DeRaad
    F. Gilmore

CODE 1220
                    1 COPY

Code 2628   22 copies
Records   1 copy

SCIENCE APPLICATIONS INTERNAT.
    CORP.
1710 Goodridge Drive
McLean, VA 22101
    E. Hyman
    K. Papadopoulos

SCIENCE APPLICATIONS INTERNAT.
    CORP.
P.O. Box 2351
San Diego, CA 92038

SRI INTERNATIONAL
333 Ravenswood Ave.
Menlo Park, CA 94025
    W. Chesnut

TOYON RESEARCH CORPROATION
P.O. Box 6890
Santa Barbara, CA 93111
    J. Ise

UNIVERSITY OF CALIFORNIA
    AT LOS ANGELES
Department of Physics
Los Angeles, CA 90024
    J.M. Cornwall
    R. Stenzel
    W. Gakelman
    A.Y. Wong
    J. Dawson

UNIVERSITY OF WISCONSIN
Fusion Technology Inst.
Madison, WS 53706
    G. Moses
    R. Peterson

VISIDYNE INC.
5 Corporate Place
South Bedford St.
Burlington, MA 01803
    J. Carpenter

4730 - 25 copies
Please send remainder of
copies to Code 4732.

DIRECTOR OF RESEARCH
U. S. NAVAL ACADEMY
ANNAPOLIS, MD 21402
                    2 COPIES

42